AIAA JOURNAL
Vol. 38, No. 6, June 2000

Shock-Shape Alteration Caused by Interaction with Organized Structures

G. Erlebacher* and M. Y. Hussaini†
Florida State University, Tallahassee, Florida 32306-4120

The dynamics of shock waves interacting with organized structures such as a vortex or a temperature spot are examined. In particular, the shock structure, i.e., its shape and velocity, is investigated. Appropriate scalings in some asymptotic limits are derived for the shock displacement and velocity in terms of the upstream Mach number and the amplitude of the vortex or temperature spot. Two sources of nonlinearity are identified, and their effect on the dynamics of shocks are studied. Some light is shed on the incipient stage in the formation of branch points.

Nomenclature

c = speed of sound
e = internal energy
M = Mach number
$\boldsymbol{n}$ = unit vector normal to the shock
p = pressure
R = universal gas constant
r_0 = characteristic length scale of upstream structure
s = entropy
T = temperature
t = time
U = mean streamwise velocity
$\boldsymbol{u}$ = velocity vector
u, v = streamwise, normal velocity
v_θ = azimuthal velocity in upstream vortex
x, y = directions normal and tangential to the steady shock
γ = ratio of specific heats
Δ = displacement
δ = $(\boldsymbol{u} - \boldsymbol{u}_s) \cdot \boldsymbol{n}$
ϵ = perturbation amplitude
ζ = ρc
ρ = density

Subscripts

L = downstream boundary
s = shock
s = relative to upstream flow
0 = dimensional reference value
1 = upstream

Superscripts

$*$ = scaled time
$'$ = perturbation variable
$(\bar{\ })$ = mean value

Introduction

THE interaction of vortices and other flow structures with shock waves is an area of fundamental interest in fluid mechanics. As such, several investigations in the past few years have concentrated on identifying these mechanisms and studying them in isolation.[1–9] The theory is necessarily linear,[6] although it appears to hold up surprisingly well in regimes where one may intuitively feel that its basic assumptions break down. Some numerical simulations have established the limit for the range of validity of the linear theory.[1,5,7] For example, when a transverse vortex interacts with a shock, it has been established that the linear theory breaks down when the product of vortex circulation and upstream Mach number is of order unity.

Several experimental[8,9] and numerical[10,11] studies have observed triple points and secondary shocks; however, these have been restricted to relatively low Mach numbers (less than 1.3) and were based on shock-capturing numerical techniques, which prevent a detailed analysis of the flow properties along the shock.

The present work focuses on the dynamics of shocks, including their shape and velocity profiles, which are influenced by not just the flow upstream but also by the flow downstream of the shock. We concentrate on a range of upstream Mach numbers from 2 to 10. To this end, the equation for the shock evolution is solved along with the Euler equations downstream of the shock. The behavior of the shock displacement and shock velocity is deduced in the asymptotic limit of low amplitude and high Mach number. These observations are then substantiated by numerical results. For a given shock strength, if the upstream disturbance is sufficiently strong, the shock may develop what is called a branch point or a triple point, which is the confluence of three shocks. This is reminiscent of irregular shock reflection with a Mach stem,[12] although the mechanisms at play here are quite different in nature. It appears that the upstream-propagating acoustic waves (in the downstream region) interacting with the shock lead to the formation of branch points in certain situations. Although the simulations fit the main shock, they try to capture the secondary shocklet. Inherent lack of resolution, together with the high order of the numerical method, manifests itself in the simulations as numerical oscillations. We attempt to make a systematic study of this configuration within the constraint of the current resolutions to arrive at reasonable conclusions as to the formation and propagation of these branch points.

The paper is organized in five sections. The first is the introduction. The second section briefly defines the problem and succinctly describes the method of solution, which is described in detail in earlier publications. The third section analyzes the Rankine–Hugoniot conditions and the shock evolution equation and deduces the shock characteristics in the limit of low amplitude and high Mach number. It also includes some observations about the propagation of wavelike disturbances along the shock. The fourth section presents the detailed simulation results pertaining to the shock shape and its velocity profile, appearance of branch points, and their propagation. The fifth and final section provides some conclusions.

Problem Statement and Solution Technique

We consider the effect of an oncoming two-dimensional disturbance on an otherwise plane steady shock initially at $x = 0$. The flow upstream of the shock consists of a vortex or temperature spot superimposed on a uniform stream with velocity U_0 normal to the

Received 4 May 1999; revision received 20 September 1999; accepted for publication 16 November 1999.

*Associate Professor, Department of Mathematics and Computational Science and Information Technology. Senior Member AIAA.
†Eminent Scholar and Director, School of Computational Science and Information Technology.

undisturbed shock, pressure P_0, and temperature T_0. In the region between the shock front $x = x_s(y, t)$ and the far downstream boundary at $x = x_L$, we seek the solution of the two-dimensional compressible Euler equations

$$\frac{\partial \rho}{\partial t} + \nabla \cdot (\rho \boldsymbol{u}) = 0 \tag{1}$$

$$\frac{\partial (\rho \boldsymbol{u})}{\partial t} + \nabla \cdot (\rho \boldsymbol{u}\boldsymbol{u}) = -\nabla p \tag{2}$$

$$\frac{\partial}{\partial t}\left(\rho e + \frac{1}{2}\rho \boldsymbol{u}^2\right) + \nabla \cdot \left(\rho \boldsymbol{u}\left(e + \frac{1}{2}\boldsymbol{u}^2\right) + p\boldsymbol{u}\right) = 0 \tag{3}$$

where $e = [(\gamma - 1)\rho]^{-1} p$ is the internal energy per unit mass for an ideal gas.

Density, pressure, and temperature are made nondimensional with respect to their respective undisturbed upstream values ρ_0, P_0, and T_0. Velocity $\boldsymbol{u} = (u, v)$ is nondimensionalized with respect to $(RT_0)^{1/2}$, where R is the ideal gas constant. Therefore, the mean upstream velocity $|\bar{u}_1| = M_1 \sqrt{\gamma}$, where $M_1 = U_0/(\gamma RT_0)^{1/2}$ and γ is the ratio of the specific heats assumed equal to 1.4 for air. Length scales are normalized with respect to the characteristic length r_0 of the upstream disturbance, and time is normalized with respect to r_0/U_0.

Equations (1–3) are solved along with an evolution equation for the shock[1,2]:

$$(n_x u_s)_{,t} = [D + \zeta(1 - A)]^{-1}[(D - \zeta A)(\boldsymbol{n} \cdot \boldsymbol{u}_1)_{,t} + \zeta(\boldsymbol{u} \cdot \boldsymbol{n}_{,t}) + (E - \zeta B)p_{1,t} + (F - \zeta C)\rho_{1,t} - \mathcal{R}] \tag{4}$$

where $u_s = x_{s,t}(y, t)$, $\zeta = -\rho c$, c is the nondimensional sound speed,

$$\boldsymbol{n} = (n_x, n_y) = \left[\frac{1}{\left(1 + x_{s,y}^2\right)^{\frac{1}{2}}}, \frac{-x_{s,y}}{\left(1 + x_{s,y}^2\right)^{\frac{1}{2}}}\right] \tag{5}$$

is the unit vector normal to the shock, and

$$\mathcal{R} = \zeta \boldsymbol{n} \cdot (\boldsymbol{u} \cdot \nabla \boldsymbol{u} + \nabla p/\rho) - (\boldsymbol{u} \cdot \nabla p + \gamma p \nabla \cdot \boldsymbol{u}) \tag{6}$$

The coefficients A through F are

$$A = \frac{\gamma - 1}{\gamma + 1} - \frac{2\gamma}{\gamma + 1}\frac{p_1}{\rho_1 \delta_1^2}, \qquad B = \frac{2\gamma}{\gamma + 1}\frac{1}{\rho_1 \delta_1}$$

$$C = -B\frac{p_1}{\rho_1}, \qquad D = \frac{4\rho_1 \delta_1}{\gamma + 1}$$

$$E = \frac{1 - \gamma}{\gamma + 1}, \qquad F = \frac{2\delta_1^2}{\gamma + 1} \tag{7}$$

where $\delta_1 = \boldsymbol{u} \cdot \boldsymbol{n} - u_s n_x$.

Using the analytically prescribed upstream flow, the Rankine–Hugoniot conditions provide the boundary conditions at the right domain boundary $x = x_s(y, t)$. At the left boundary $x = x_L$ a nonreflecting boundary condition is applied using the so-called buffer zone technique.[13] The top and bottom boundaries are sufficiently far removed from the exponentially decaying perturbations so that all perturbations may be set to zero.

It is convenient to transform the time variable as

$$t^* = |\bar{u}_1| t - x_c$$

so that the center of an upstream structure initially centered at $(x, y) = (x_c, 0)$ crosses the shock at $t^* = 0$, whereas its edges cross the shock at $t^* = \pm 1$.

Vortex

The transverse vortex initially centered at $x = x_c$ (convected with the mean upstream velocity $\bar{u}_1$) has an azimuthal velocity

$$v_{\theta 1} = (\epsilon r/2\pi)\, e^{\frac{1}{2}(1 - r^2)} \tag{8}$$

The nondimensional circulation is

$$\int_0^{2\pi} v_{\theta 1} r \, \mathrm{d}\theta = \epsilon$$

evaluated at $r = 1$. The dimensional circulation is $(RT_0)^{1/2} r_0 \epsilon$. The flowfield is assumed to be isentropic with density

$$\rho = T_1^{1/(\gamma - 1)} \tag{9}$$

and temperature

$$T_1 = 1 - \frac{(\gamma - 1)\epsilon^2}{8\gamma\pi^2} e^{1 - r^2} \tag{10}$$

where the radial coordinate

$$r^2 = (x + t^*)^2 + y^2 \tag{11}$$

The vortex rotates counterclockwise when $\epsilon > 0$ and counterclockwise when $\epsilon < 0$.

Temperature Spot

The temperature spot has no associated velocity field and has a perturbation temperature profile

$$T_1 = 1 + \epsilon e^{-\frac{1}{2}r^2} \tag{12}$$

with r^2 defined by Eq. (11). Pressure is assumed to be uniform, whereas the density

$$\rho = T_1^{-1} \tag{13}$$

is determined from the equation of state. Both the vortex and the temperature spot satisfy the time-dependent Euler equations.

The numerical algorithm used to solve Eqs. (1–4) is described in detail elsewhere.[1] Briefly stated, the spatial derivatives are discretized with a formally sixth-order-accurate compact method[14] in both coordinate directions, whereas time advancement is based on a third-order, low-storage Runge–Kutta scheme.[15] The governing equations (1–3) are solved along with the shock evolution equation (4). The domain of computation for the shock/vortex interaction problem encompasses the region $(x, y) \in ([-3.33, 10.5], [-50, 50])$ with a grid resolution of 250×150. The center of the vortex is initially at $x_c = 15$. The computational domain for the temperature spot case is $(x, y) \in ([-20, 0], [0, 23])$. Symmetry conditions about $y = 0$ are applied in the direction parallel to the shock. All of the temperature spot simulations presented in this paper have a grid resolution of 331×64. The center of the spot is initially at $x_c = 5$. In both cases the grid is uniform in x and stretched in y.[1,2]

The current code has been checked extensively against the analytical predictions of linear theory.[1] In that study incoming plane vorticity waves were allowed to interact with the shock to produce plane acoustic, entropy, and vorticity waves. The numerical results were checked against linear theory by comparing the wave amplitudes as a function of the downstream distance from the shock. For upstream wave amplitudes of 0.01% of the mean streamwise velocity, the computed results agreed with linear theory to within 0.1% when there are 6–10 points per wavelength in the downstream region. The results were confirmed by considering the discretization error of the derivative of $\sin(kx)$. The conclusion was made that to obtain a relative error of 0.1% requires approximately 10 uniformly spaced grid points per wavelength. These a priori estimates for resolution are followed in the current study.

Grid-convergence studies were also performed to ascertain the accuracy of the solution. Shock velocity profiles and pressure profiles along $y = 0$ were determined for the case of an incoming vortex with $\epsilon = 0.01$ on three grids—125×75, 250×150, and 500×300. We computed a relative L_2 error $\|u - u_{\text{finest}}\|_2^{1/2} / \|u_{\text{finest}}\|_2^{1/2}$ of a variable u, where u_{finest} is the solution on the finest grid. For instance,

shortly after the vortex crosses the shock ($t^* = 4$) the relative L_2 error decreased by a factor of 16, indicating fourth-order accuracy both along the shock and along the centerline. On the 250×150 grid used in the simulations, the average relative L_2 error was on the order of 0.1%, where the pressure and shock velocity have a magnitude greater than 10^{-6}. At similar upstream amplitudes the preceding resolution requirements are also satisfied for the shock-entropy interaction simulations.

Analysis

In this section we carry out an asymptotic analysis of the Rankine–Hugoniot conditions and the shock evolution equation in the limit of low upstream perturbation amplitude ϵ and upstream Mach number M_1.

Rankine–Hugoniot Relations

Following Whitham,[16] the flow variables immediately behind the shock can be expressed as a function of the upstream variables and the shock velocity according to

$$\frac{\rho}{\rho_1} = \frac{(\gamma+1)M_s^2}{(\gamma-1)M_s^2+2} \tag{14}$$

$$\frac{\delta-\delta_1}{c_1} = \frac{2\left(M_s^2-1\right)}{(\gamma+1)M_s} \tag{15}$$

$$\boldsymbol{u}\cdot\boldsymbol{t} = \boldsymbol{u}_1\cdot\boldsymbol{t} \tag{16}$$

$$\frac{p-p_1}{p_1} = \frac{2\gamma\left(M_s^2-1\right)}{\gamma+1} \tag{17}$$

where $\delta = \boldsymbol{n}\cdot\boldsymbol{u} - u_s n_x$ is the flow velocity normal to the shock relative to the shock, $\boldsymbol{t}$ is the unit vector tangent to the shock,

$$M_s = |\delta_1|/c_1$$

is the Mach number of the shock relative to the upstream flow, and c_1 is the velocity of sound ahead of the shock.

Small-Amplitude Expansion

Consider a small disturbance $(\boldsymbol{u}_1', p_1', \rho_1')$ superimposed on a mean upstream state $(\bar{\boldsymbol{u}}_1, \bar{p}_1, \bar{\rho}_1)$. A straightforward linearization of the Rankine–Hugoniot conditions for velocity [Eqs. (15) and (16)] and pressure [Eq. (17)] takes the form

$$\frac{u'-u_1'}{\bar{c}} = \frac{2\left(M_1^2-1\right)}{(\gamma+1)M_1}\frac{c'}{\bar{c}} \tag{18}$$

$$+\frac{2}{\gamma+1}\frac{\bar{c}_1}{\bar{c}}\frac{M_1^2+1}{M_1^2}M_s' \tag{19}$$

$$v/\bar{c} = v_1/\bar{c} + (\bar{\rho}/\bar{\rho}_1 - 1)M_1 x_{s,y} \tag{20}$$

$$\frac{p'}{\bar{p}} = \frac{p_1'}{\bar{p}_1}\frac{\bar{p}}{\bar{p}_1} + \frac{4\gamma}{\gamma+1}M_1 M_s' \tag{21}$$

The perturbations of relative Mach number M_s and sound speed c satisfy

$$M_s' = \frac{u_s'-u_1'}{\bar{c}_1} - M_1\frac{c_1'}{\bar{c}_1} \tag{22}$$

$$2\frac{c_1'}{\bar{c}_1} = \frac{\gamma-1}{\gamma}\frac{p_1'}{\bar{p}_1} + \frac{s_1'}{\gamma} \tag{23}$$

where s_1' is the perturbation upstream entropy

$$s_1' = p_1'/\bar{p}_1 - \gamma\rho_1'/\bar{\rho}_1 \tag{24}$$

Substituting Eqs. (22–24) into the linearized Rankine–Hugoniot relations (18–21) and rearranging terms to normalize upstream and downstream perturbations with respect to their respective mean values finally leads to

$$\frac{u'-u_s}{\bar{u}} = \frac{(\gamma-1)M_1^2-2}{(\gamma-1)M_1^2+2}\frac{u_1'-u_s}{\bar{u}_1}$$

$$+\frac{2}{\gamma(\gamma+1)M_1^2}\frac{\bar{\rho}}{\bar{\rho}_1}\left((\gamma-1)\frac{p_1'}{\bar{p}_1}+s_1'\right) \tag{25}$$

$$\frac{v'}{\bar{u}} = \frac{\bar{\rho}}{\bar{\rho}_1}\frac{v_1'}{\bar{u}_1} - \left(\frac{\bar{\rho}}{\bar{\rho}_1}-1\right)x_{s,y} \tag{26}$$

$$\frac{p'}{\bar{p}} = \left(\frac{2M_1^2-(\gamma-1)}{2\gamma M_1^2-(\gamma-1)}\right)\frac{p_1'}{\bar{p}_1}$$

$$-\frac{2M_1^2}{\gamma+1}\frac{\bar{p}_1}{\bar{p}}s_1' + \frac{4\gamma M_1^2}{\gamma+1}\frac{\bar{p}_1}{\bar{p}}\frac{u_1'-u_s}{\bar{u}_1} \tag{27}$$

High-Mach-Number Expansion

In the limit of high Mach number, the Rankine–Hugoniot (R-H) relations (14–17) simplify to

$$\bar{u}_1/\bar{u} = \bar{\rho}/\bar{\rho}_1 = (\gamma+1)/(\gamma-1) \tag{28}$$

$$\bar{p}/\bar{p}_1 = 2\gamma M_1^2|\ (\gamma+1) \tag{29}$$

In the large-Mach-number limit the linearized R-H relations (25–27) using the preceding expressions, lead to

$$\frac{u'-u_s}{\bar{u}} = \frac{u_1'-u_s}{\bar{u}_1} + \frac{2}{\gamma(\gamma-1)M_1^2}\left((\gamma-1)\frac{p_1'}{\bar{p}_1}+s_1'\right) \tag{30}$$

$$\frac{v'}{\bar{u}} = \frac{\gamma+1}{\gamma-1}\frac{v_1'}{\bar{u}_1} + \frac{2}{\gamma-1}x_{s,y} \tag{31}$$

$$\frac{p'}{\bar{p}} = \frac{p_1'}{\gamma\bar{p}_1} - \frac{s_1'}{\gamma} + 2\frac{u_1'-u_s}{\bar{u}_1} \tag{32}$$

Shock Evolution Equation

To help determine the scaling of shock and downstream variables with respect to the upstream perturbation amplitude and the upstream Mach number, it is necessary to derive the linearized form of the shock evolution equation (4). In the limit of high M_1 and small ϵ, Eq. (4) becomes

$$\left(\frac{\bar{c}}{\bar{c}_1}\frac{1}{\gamma-1}+\frac{2}{\gamma+1}M_1\right)\frac{\partial u_s}{\partial t^*}2\bar{\rho}_1\bar{c}_1|\bar{u}_1| \qquad (A)$$

$$+\left(\frac{\bar{c}}{\bar{c}_1}-\frac{4}{\gamma+1}M_1\right)\frac{\partial u_1'}{\partial t^*}\bar{\rho}_1\bar{c}_1|\bar{u}_1| \qquad (B)$$

$$+\frac{2M_1^2\bar{p}_1|\bar{u}_1|}{\gamma+1}\left(\frac{\partial}{\partial t^*}\left(\frac{p_1'}{\bar{p}_1}\right)-\frac{\partial s_1'}{\partial t^*}\right) \qquad (C)$$

$$+\gamma\bar{p}\frac{\partial v'}{\partial y} + \overline{\rho c}(\bar{u}+\bar{c})\frac{\partial u'}{\partial x} + (\bar{u}+\bar{c})\frac{\partial p'}{\partial x} = 0 \tag{33}$$

(Lower-order terms proportional to $\partial p_1/\partial t$ have been neglected.) Terms that include upstream contributions are labeled A through C. As a function of the upstream Mach number and the flow variables, they have the scalings $A \propto u_s M_1^2$, $B \propto u_1 M_1^2$, $C \propto M_1^3 \max(p_1', s_1')$.

Scaling of Shock Velocity and Shock Displacement

In previous papers[1–3] we deduced the scaling of the shock amplitude and velocity from numerical results and heuristic arguments. However, a proper balance of terms in the shock evolution equation produces the correct scalings in a natural way. In the absence of upstream perturbations, the shock is plane and steady. As a disturbance is convected through the shock, the shock acquires just the right amount of velocity to ensure that its shape remains consistent with the newly forming structures in the downstream region. In turn, they interact with the shock through the information carried by the upstream-pointing acoustic characteristics. This interaction has been taken into account in the derivation of the shock evolution equation. Thus, at early times the motion of the shock is primarily determined by the dominant upstream terms in Eq. (33). After the

upstream disturbance clears the shock, the shock velocity is solely determined by the properties of the downstream flow at the shock.

We estimate the magnitude of each term in the shock evolution equation during the period $t^* \in [-1, 1]$, the time it takes the upstream disturbance to cross the shock. We consider in turn an upstream vorticity patch and an upstream entropy spot and deduce the scalings of u_s with respect to M_1 and ϵ.

Vorticity Patch

Both streamwise and tangential upstream perturbation velocities are $\mathcal{O}(\epsilon)$, whereas the pressure field (which balances the centrifugal force) is $\mathcal{O}(\epsilon^2)$. At early times the shock motion is predominantly driven by the upstream flow. Therefore, the terms in Eq. (33), which must balance, are A, B, C. The upstream thermodynamic effects (C) are negligible when $u_1' M_1^2 \gg p_1' M_1^3$ or $\epsilon M_1 \ll 1$. They first contribute to the leading-order balance when $\epsilon M_1 = \mathcal{O}(1)$. In this case the upstream flow has $\mathcal{O}(\epsilon)$ and $\mathcal{O}(\epsilon^2)$ contributions. Balancing terms A and C implies that $u_s M_1^2 \propto p_1' M_1^3$ so that $u_s = \mathcal{O}(\epsilon M_1)$. The quadratic contributions constitute a source of nonlinearity. Thus, the curve

$$\epsilon M_1 = 1 \tag{34}$$

separates regions in parameter space where the linear assumption is valid from the regions where nonlinear effects must be taken into account.[1] The only term that includes the shock velocity is $A \propto u_s M_1^2$. In the linear regime $u_s \propto u_1' = \mathcal{O}(\epsilon)$.

Figure 1 shows the shock velocity profiles u_s normalized by ϵ at different times for $M_1 = 2$, 5, 8, and $\epsilon = 0.03$ (linear regime). The magnitude of the shock velocity at $M_1 = 5$ and 8 are of the same order, which confirms the predicted scaling. From the scaling of the shock velocity, it immediately follows that the shock displacement is $\mathcal{O}(\epsilon / M_1)$.

Entropy Spot

The upstream flow is void of vorticity, and the entropy spot has a constant pressure profile. Only terms A and C in Eq. (33) represent nonzero upstream effects, and so they must balance. There are no additional constraints on ϵ. Nonlinear effects cannot be deduced from this equation unless higher-order terms are included in the original Taylor expansion of the R-H relations with respect to ϵ. From the balance of A and C, $u_s M_1^2 \propto M_1^3 p_1'$, and the shock velocity is $\mathcal{O}(\epsilon M_1)$. This result is consistent with the scalings obtained for the vorticity patch when $\epsilon M_1 \gg 1$. Indeed, the influence of the upstream vortex velocity field on u_s then becomes negligible compared to that of the pressure core (of amplitude ϵ^2), which generates $\mathcal{O}(M_1^2)$ effects downstream of the shock. In this case $u_s = \mathcal{O}(\epsilon^2 M_1)$, which is identical to the scaling of u_s produced by an entropy spot of amplitude ϵ^2.

Shock velocity profiles resulting from the interaction of a shock with a two-dimensional entropy spot of amplitude $\epsilon = 10^{-4}$ are shown in Fig. 2 at different times for $M_1 = 2$, 5, 8. The velocity is normalized by ϵM_1. The collapse of the Mach 5 and 8 curves confirm the predicted scaling. As a result, the displacement of the shock is $\mathcal{O}(\epsilon)$.

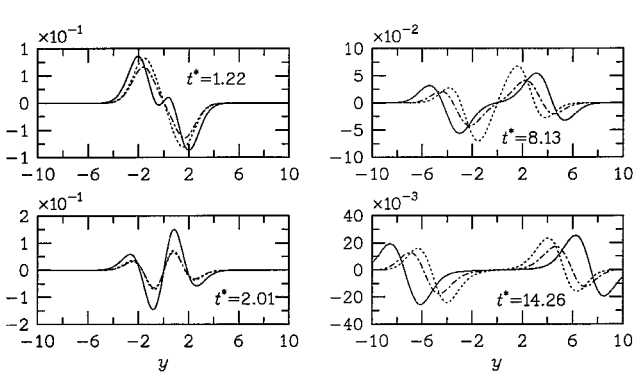

Fig. 1 Scaled shock velocity $\epsilon^{-1} u_s$ at $M_1 = 2$ (——), $M_1 = 5$ (····), and $M_1 = 8$ (– –). Vortex, $\epsilon = 0.03$.

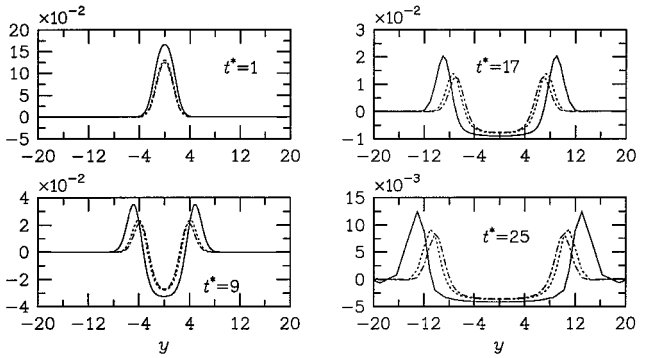

Fig. 2 Scaled shock velocity $(\epsilon M_1)^{-1} u_s$ at $M_1 = 2$ (——), $M_1 = 5$ (····), and $M_1 = 8$ (– –). Temperature spot, $\epsilon = 10^{-4}$.

Shock Shape and Velocity Profiles

In this section we examine the time history of shock velocity and displacement profiles and relate their characteristics to the pertinent initial upstream disturbance. Figures 1 and 2 show that after the initial interaction of the upstream structure with the shock a wavelike perturbation in the shock shape propagates away from $y = 0$ toward the freestream. To explain this feature, we appeal to Ribner's linear theory, which describes the interaction of a shock with a vortex.[17] Ribner computed the structure of the acoustic wave downstream of a shock interacting with a two-dimensional vortex of infinitesimal amplitude. He showed that the shape of the acoustic wave is nearly circular and propagates outward from its center at the mean speed of sound. The center of the acoustic wave convects at the mean velocity $\bar{u}$ along $y = 0$. Therefore, to leading order in ϵ, the intersection point y_w of the shock with the acoustic front has a velocity

$$c_w = \bar{c}(1 - M^2)^{\frac{1}{2}} \tag{35}$$

which at high M_1 becomes

$$c_w = [(\gamma - 1)/(\gamma + 1)]^{\frac{1}{2}} \bar{c}_1 M_1 \approx 0.4 \bar{c}_1 M_1 \tag{36}$$

In units of t^*, the velocity c_w^* of the interaction point y_w (the propagation velocity of the shock-shape perturbation) is

$$c_w^* = \frac{\mathrm{d}y_w}{\mathrm{d}t^*} = \frac{c_w}{\bar{c}_1 M_1} \tag{37}$$

which asymptotes to 0.4 as $M_1 \to \infty$. At $M_1 = 2$, $c_w^* = 0.53$; at $M_1 = 8$, $c_w^* = 0.42$.

We now examine in detail the structure of the shock velocity profile $u_s(y, t)$ and the shock displacement profile $\Delta x_s(y, t)$ as a function of time when the initial upstream disturbance is either an isentropic transverse vortex or a two-dimensional entropy spot.

Vorticity Patch

Figures 3 and 4 show shock velocity profiles at several times. Each plot presents u_s for four different values of ϵ. The shock velocity is normalized by ϵ / t^* to scale out the expected $1/t^*$ decay law[17] of the acoustic wave when $t^* \gg 1$. Deviation from the $\epsilon = 0.03$ curve directly measures the effect of nonlinearities on the shock velocity profile. As expected from Eq. (34), at fixed ϵ nonlinear effects are stronger at higher Mach number. When $t^* = 4$ and $\epsilon = 1$, oscillations appear in the shock velocity profile in the vicinity of $y = 1$ (Fig. 3). This suggests the formation of a singularity in u_s. Two singularities are clearly visible in the figure; they correspond directly to a discontinuous slope in the shock displacement profile. These points, called branch points or triple points, result from the inability of the primary and refracted shocks to adjust to the local downstream flow conditions leading to a secondary shock. The two triple points propagate in opposite directions toward the freestream. Although the higher value of ϵM_1 at $M_1 = 8$ suggests stronger nonlinear effects, there are no discernible singularities in the shock velocity profiles by $t^* = 8$ (Fig. 4). By $t^* = 10$, however, small oscillations in the shock velocity profiles suggest that a singularity may be forming along the shock. The maximum amplitude of u_s remains approximately constant for $t^* > 6$, which confirms the predicted $1/t^*$ scaling law.

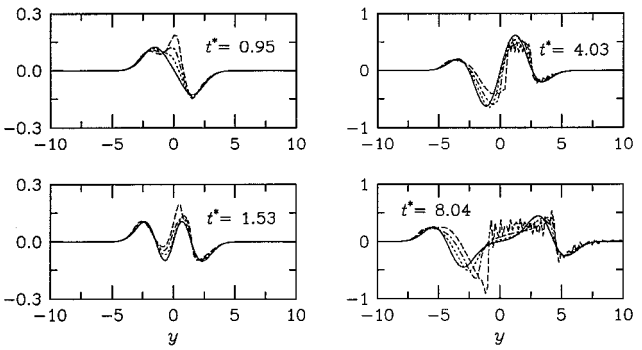

Fig. 3 Profiles of scaled shock velocity $\epsilon^{-1}t^*u_s$ at different t^*. $\epsilon = 0.03$ (——), 0.3 (····), 0.6 (– –), and 1.0 (– – –). Transverse vortex, $M_1 = 2$.

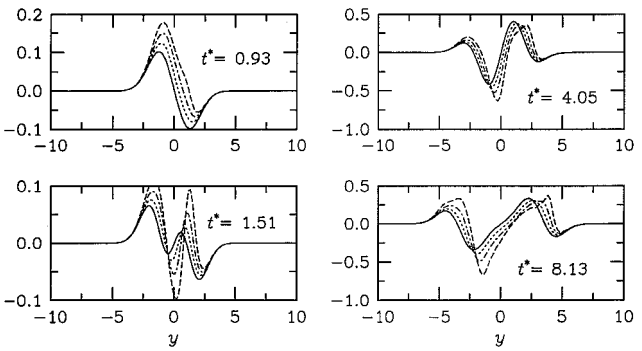

Fig. 4 Profiles of scaled shock velocity $\epsilon^{-1}t^*u_s$ at different t^*. $\epsilon = 0.03$ (——), 0.3 (····), 0.6 (– –), and 1.0 (– – –). Transverse vortex, $M_1 = 8$.

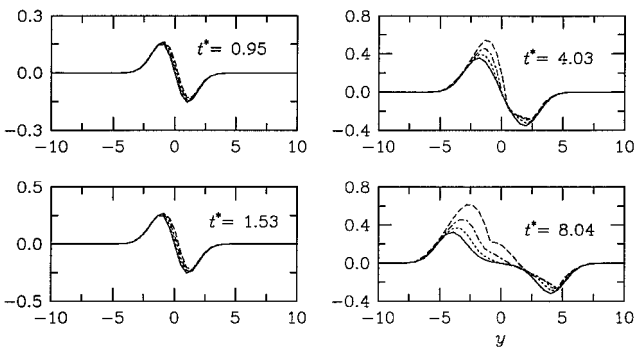

Fig. 5 Profiles of scaled shock displacement $\epsilon^{-1}M_1t^*\Delta x_s$ at different t^*. $\epsilon = 0.03$ (——), 0.3 (····), 0.6 (– –), and 1.0 (– – –). Transverse vortex, $M_1 = 2$.

Shock displacement profiles $\Delta x_s = x_s(y, t) - x_s(y, 0)$ at Mach 2 and 8 are shown in Figs. 5 and 6, respectively. The two triple points in the shock velocity profile at Mach 2 appear in Fig. 5 as kinks in the shock. They are clearly visible at $t^* = 4$. When $t^* < 1$ (i.e., before the vortex completely clears the shock), the shock displacement profiles have approximately the same shape and amplitude at both Mach numbers under linear conditions. Their shape is roughly antisymmetric with respect to $y = 0$, which is consistent with the antisymmetry of the upstream velocity field and the negligible influence of the $\mathcal{O}(\epsilon^2)$ perturbation pressure field in the vortex core. At higher ϵ the profiles become asymmetric. At low Mach numbers the loss of antisymmetry is predominantly caused by nonlinear convective effects. At high Mach numbers the dominant cause for the loss of antisymmetry is the presence of the symmetric upstream pressure perturbation within the vortex, which can no longer be neglected. In this case the effects of p_1' and u_1' on the properties of the downstream flow are of the same order.

To pinpoint unambiguously the source of the observed nonlinearities, we conduct several numerical experiments designed to isolate the effects of the upstream velocity and pressure fields on the structure of the shock. In addition to the full upstream vortex (referred to as S1), we consider two flows not physically realizable. If the

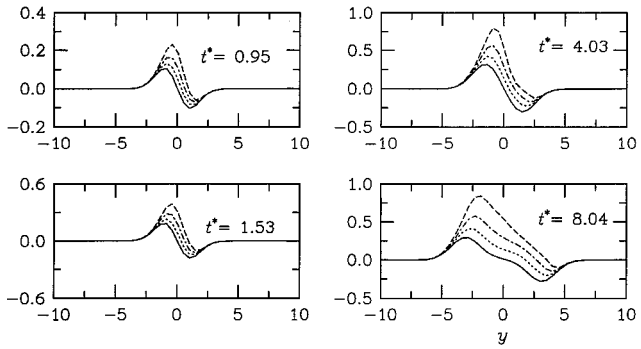

Fig. 6 Profiles of scaled shock displacement $\epsilon^{-1}M_1t^*\Delta x_s$ at different t^*. $\epsilon = 0.03$ (——), 0.3 (····), 0.6 (– –), and 1.0 (– – –). Transverse vortex, $M_1 = 8$.

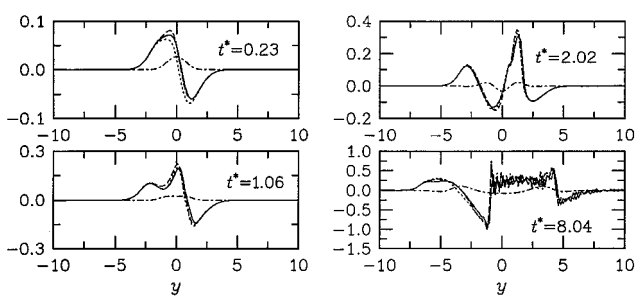

Fig. 7 Profiles of scaled shock velocity $\epsilon^{-1}t^*u_s$ at $M_1 = 2$ for full vortex (S1: ——), no pressure field (S2: ····), no velocity field (S3: – –), and sum of S2 and S3 at $\epsilon = 1$ (S4: – – –).

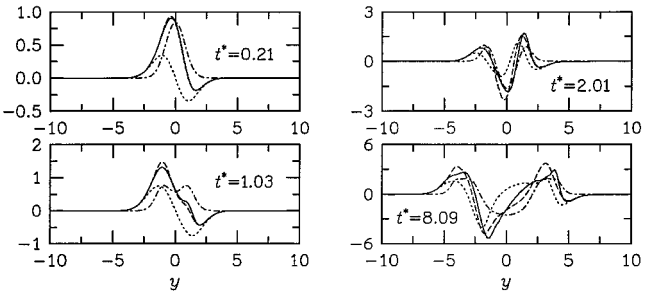

Fig. 8 Profiles of scaled shock velocity $\epsilon^{-1}t^*u_s$ at $M_1 = 8$ for full vortex (S1: ——), no pressure field (S2: ····), no velocity field (S3: – –), and sum of S2 and S3 at $\epsilon = 1$ (S4: – – –).

pressure perturbation associated with the vortex core is neglected, the upstream flow is linear in ϵ, which is the case considered by Ribner,[6] who considered a vortex of infinitesimal amplitude. The neglect of the pressure field, which scales as ϵ^2, is then justified. As $\epsilon \to 0$, S2 and S1 become identical. Finally, when the velocity field is set to zero, leaving the thermodynamic field intact, the resulting experiment is labeled S3. For comparison with S1, we sum the results from S2 and S3 and call it S4. The difference between S1 and S4 is a measure of nonlinearity. Although the upstream flows defined by S2 and S3 do not satisfy the steady-state Euler equations, they are nonetheless advected at the upstream mean velocity into the shock to permit a consistent comparison with the full vortex case S1. The resulting shock velocity profiles are presented in Figs. 7 and 8 for $\epsilon = 1$ at $M_1 = 2$ and 8, respectively. The shock velocity in S3 is symmetric about $y = 0$ for all time. This is to be expected because the nonlinear Euler equations preserve the symmetry of the thermodynamic fields if they are initially symmetric, assuming that the boundary conditions are symmetric. The downstream streamwise velocity is symmetric, and the velocity component parallel to the mean shock is antisymmetric. In contrast, the antisymmetry of u_1' in S2 is destroyed because of the effect of the quadratic convective nonlinearities in the Euler equations. Antisymmetry is clearly broken by $t^* = 0.5$ (not shown) before the vortex has fully crossed the shock. At Mach 8 shock velocity profiles for S2 also lack an

antisymmetric structure but to a lesser degree than at Mach 2. It is approximately maintained past $t^* = 1$ but is clearly lost by $t^* = 2$.

In the absence of an upstream velocity field (S3), linear theory predicts that when $u_1' = 0$, $u_s \propto \epsilon^2 M_1$, $\Delta x_s \propto \epsilon^2$. On the other hand, when $p_1' = 0$, $u_s \propto \epsilon$ and $\Delta x_s \propto \epsilon M_1^{-1}$. Neglecting the nonlinear interaction between the solutions S2 and S3, it is clear that the shock velocity in S3 is that of S2 multiplied by ϵM_1. As a consequence, when $\epsilon M_1 \ll 1$ the effect of p_1' on the shock profiles can safely be neglected. Figure 8 confirms that the effect of p_1' is stronger at $M_1 = 8$ than at $M_1 = 2$ for a fixed vortex circulation.

Although not shown, by $t^* = 6$, p_1' accounts for more than 20% of the shock displacement amplitude at $M_1 = 2$. At Mach 8, p_1' cannot be neglected; its effect on Δx_s is actually stronger than that of u_1'. This is consistent with $\epsilon M_1 > 1$.

A close examination of Fig. 8 reveals that the shock velocity profiles that correspond to S4 (S2 + S3) closely approximate the profile in S1 (full vortex), with similar conclusions for the shock displacement. In other words, a linear superposition of the nonlinear contributions of S2 and S3 gives a shock velocity and displacement that is close to that associated with the upstream vortex. As a first approximation therefore, the upstream vortical and thermodynamic components can be treated separately, and the results superimposed to obtain the physical flowfield. This perhaps holds the key to a new theoretical framework applicable to nonlinear interactions at high Mach numbers.

Entropy Spot

In this section we consider the interaction of an entropy spot, which convects at the mean upstream velocity, with a stationary shock and contrast it with S3. Both u_1' and p_1' are set to zero. The upstream entropy perturbation is

$$s_1' = \gamma^{-1} T_1' = \mathcal{O}(\epsilon_{\text{spot}})$$

Experiment S3 on the other hand considered an upstream flow with a constant velocity field and an isentropic thermodynamic field. The lack of a perturbation velocity field in these two flows suggests that their effect on the structure of the shock be compared. (In the following, we add subscripts *vortex* and *entropy* to the amplitude ϵ to distinguish between the two kinds of upstream disturbances.)

The effect of an upstream perturbation on the shock is ascertained by a careful examination of the R-H conditions and the shock evolution equation. After setting u_1' to zero, the linearized R-H conditions (30–32) become

$$\frac{u' - u_s}{\bar{u}} = -\frac{u_s}{\bar{u}_1} + \frac{2}{\gamma M_1^2}\frac{p_1'}{\bar{p}_1} \tag{38}$$

$$v'/\bar{u} = [2/(\gamma - 1)]x_{s,y} \tag{39}$$

$$p'/\bar{p} = p_1'/\gamma\bar{p}_1 - 2(u_s/\bar{u}_1) \tag{40}$$

for S3, and

$$\frac{u' - u_s}{\bar{u}} = -\frac{u_s}{\bar{u}_1} + \frac{2}{\gamma(\gamma - 1)M_1^2}s_1' \tag{41}$$

$$v'/\bar{u} = [2/(\gamma - 1)]x_{s,y} \tag{42}$$

$$p'/\bar{p} = -(s_1'/\gamma) - 2(u_s/\bar{u}_1) \tag{43}$$

for the entropy spot in the high M_1 limit. To simplify these expressions further, recall that if $u_1' = 0$ a balance of terms in the high-Mach-number limit of the linearized shock evolution equation (33) led to the conclusion that $u_s = \mathcal{O}(\epsilon M_1)$. Therefore, the thermodynamic term in Eqs. (38) and (41) is smaller by a factor M_1^2 than the velocity term and can be safely neglected as a first approximation. On the other hand, both terms in the equation for p' are of the same order. It follows that in the high-Mach-number limit the R-H relations take on the same form if

$$p_1'/\bar{p}_1 = -s_1' \tag{44}$$

Furthermore, p_1' and s_1' appear in the shock evolution equation in the combination

$$\frac{2M_1^2\bar{p}_1\bar{u}_1}{\gamma + 1}\left(\frac{\partial}{\partial t^*}\left(\frac{p_1'}{\bar{p}_1}\right) - \frac{\partial s_1'}{\partial t^*}\right)$$

which states that both flows affect the shock velocity similarly if Eq. (44) is satisfied. However, this result is to be expected because the R-H relations were used to derive the shock evolution equation. It is therefore plausible to expect that, for early times, the detailed characteristics of the shock profile will be qualitatively the same for the two flows. In reality the radial profile of the upstream disturbances also affect the shock shape because it is primarily responsible for the refraction of the shock wave and the degree of nonuniformity of the shock strength along the shock. Therefore, the radial profiles between the two flows must also have similar characteristics, such as length scale and rate of change, for the shock profiles to behave similarly.

A quantitative comparison of these two flows requires that the maximum amplitude of p_1' inside the vortex equal the maximum amplitude of s_1' inside the entropy spot. From Eq. (10) the initial maximum temperature amplitude inside the vortex satisfies

$$\frac{T_{1\max}'}{\bar{T}_1} = \frac{\gamma - 1}{\gamma}\frac{p_{1\max}'}{\bar{p}_1} = \frac{\epsilon_{\text{vortex}}^2(\gamma - 1)e}{8\gamma\pi^2}$$

while the maximum temperature perturbation amplitude inside the entropy spot satisfies

$$\frac{T_{1\max}'}{\bar{T}_1} = \frac{s_{1\max}'}{\gamma} = \epsilon_{\text{spot}}$$

Applying Eq. (44) at the center of the disturbance (where the amplitude is maximal) leads to

$$\epsilon_{\text{spot}} \approx 0.025\epsilon_{\text{vortex}}^2 \tag{45}$$

The highest vortex circulation we have considered is $\epsilon_{\text{vortex}} = 1$. This corresponds to a spot amplitude of $\epsilon_{\text{spot}} \approx 0.025$, well within the linear regime. Conversely, the maximum temperature perturbation in a spot of amplitude 0.25 corresponds to an isentropic vortex of circulation $\epsilon_{\text{vortex}} = 3.2$.

At sufficiently high spot amplitudes the high curvature in the refracted region of the shock prevents the downstream flow from maintaining a shock-free character. Two secondary shocks are formed symmetrically about $y = 0$. The intersection point between the primary and secondary shocks are triple points. They show up as kinks in the shock shape.

In the absence of upstream perturbation velocity, the distortion of the shock can be characterized by the degree of nonlinearity of the convective term in the downstream momentum equations and by the variation of the nonlinearity along the shock. To measure this nonlinearity, we calculate the ratio of u' to $\bar{u}$, which represents the percentage contribution of nonlinear effects to the convective term in the momentum equation. To estimate this ratio at high M_1, we make use of Eq. (41) with Eq. (28) and neglect the effect of s_1':

$$u'/\bar{u} = (u_s/\bar{u}_1)[2/(\gamma - 1)]$$

An estimate for u_s is obtained from the shock evolution equation by considering the effect of the upstream terms on the shock velocity. This leads to the relation

$$\bar{p}_1\bar{c}_1\left(\frac{\bar{c}}{\bar{c}_1}\frac{1}{\gamma - 1} + \frac{2}{\gamma + 1}M_1\right)u_s \approx \frac{M_1^2\bar{p}_1}{\gamma + 1}s_1' \tag{46}$$

Expressing s_1' as a function of T_1' and substituting the high-Mach-number relations (28) and (29) into Eq. (46), we can relate the shock velocity to the upstream temperature disturbance:

$$u_s/\bar{u}_1 \approx 0.11(T_1'/\bar{T}_1) \tag{47}$$

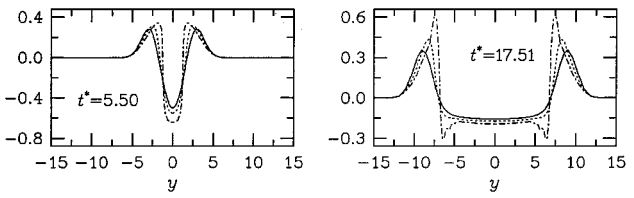

Fig. 9 Profiles of scaled shock velocity $(\epsilon M_1)^{-1} t^* u_s$ for different t^* at $\epsilon = 10^{-4}$ (——), -0.25 (···), and -0.50 (– –). Entropy spot, $M_1 = 2$.

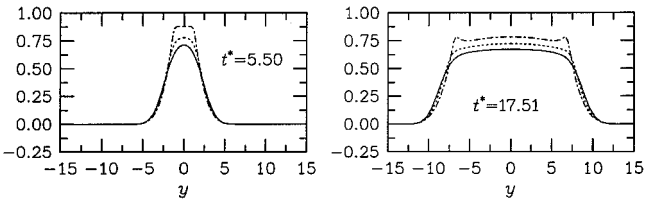

Fig. 10 Profiles of scaled shock displacement $\epsilon^{-1} t^* \Delta x_s$ for different t^* at $\epsilon = 10^{-4}$ (——), -0.25 (···), and -0.50 (– –). Entropy spot, $M_1 = 2$.

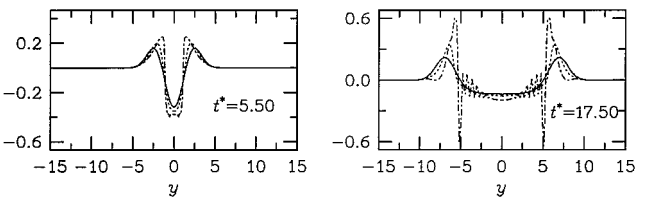

Fig. 11 Profiles of scaled shock velocity $(\epsilon M_1)^{-1} t^* u_s$ for different t^* at $\epsilon = 10^{-4}$ (——), -0.25 (···), and -0.50 (– –). Entropy spot, $M_1 = 10$.

Finally, substitution of Eq. (47) into Eq. (46) leads to the approximation

$$u'/\bar{u} \approx 0.55(T_1'/\bar{T}_1)$$

This measure of nonlinearity is independent of the upstream Mach number. When $\epsilon_{\text{spot}} = -0.25$, the nonlinear convective term $u'u_x'$ is 14% of the linear term $\bar{u}u_x'$. The fraction increases to 27% when $\epsilon_{\text{spot}} = -0.5$.

By $t^* = 5$ and for $\epsilon_{\text{spot}} = 0.5$, two triple points form along the shock velocity profile. They lie at the intersection of three shocks: the primary shock, which lies outside the region of interaction; the refracted shock, which lies between the two triple points; and the secondary shock, formed by the upstream side of the steepened acoustic front.

To substantiate the preceding estimates for the onset of strong nonlinearities, we consider the interaction of a cold spot convecting at two different Mach numbers $M_1 = 2$ and 10, each at two amplitudes $\epsilon_{\text{spot}} = -0.25$ and -0.50 into a stationary shock. A linear reference case is used for comparison ($\epsilon_{\text{spot}} = 10^{-4}$). Figure 9 shows the shock velocity profile normalized by ϵM_1 at several t^* when $M_1 = 2$. As ϵ_{spot} is increased past 0.25, two discontinuities clearly form along the shock. The formation and dynamics of these discontinuities are qualitatively different from that encountered when the shock interacts with a strong vortex. In the latter case two discontinuities form at a single point along the shock as a result of the asymmetry of the upstream azimuthal velocity. In the former case the constraint of symmetry forces the formation of two triple points along the shock, appearing symmetrically about $y = 0$, followed by their propagation (in opposite directions) toward the freestream at a rate dictated by the propagation speed of the acoustic wave. The triple points are visible at the edges of the hat-shaped profile of Δx_s (Fig. 10). We have not observed triple points in u_s in the S3 simulations. Equation (45) predicts that a vortex circulation of at least three is required for triple points to form. Shock velocity and displacement profiles at Mach 10 are similar to those at Mach 2 but with stronger discontinuities (Figs. 11 and 12).

As a general observation, u_s and Δx_s have a higher magnitude at the lower Mach number (even in the linear regime). However, nonlinear effects are somewhat stronger in the high-Mach-number

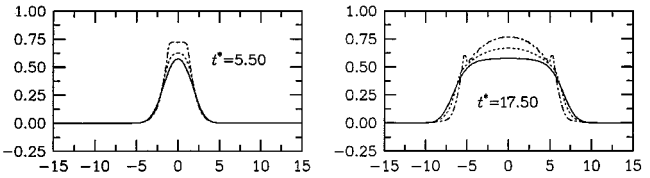

Fig. 12 Profiles of scaled shock displacement $\epsilon^{-1} t^* \Delta x_s$ for different t^* at $\epsilon = 10^{-4}$ (——), -0.25 (···), and -0.50 (– –). Entropy spot, $M_1 = 10$.

limit. The degree of nonlinearity is measured by the relative displacement of profiles from linear conditions. For $t^* \approx 5$ it appears that the departure of Δx_s from linear conditions is $\mathcal{O}(\epsilon_{\text{spot}}^2)$. However, the nonlinear effect reverts to $\mathcal{O}(\epsilon_{\text{spot}})$ once the perturbation along the shock has cleared the central region near $y = 0$.

Finally, we measure the propagation speed of the perturbations along the shock. We track the location of the peak shock velocity in time and measure the distance covered between $t^* = 11.5$ and 29.5. At Mach 2 we find $c_w^* \approx 0.5$ when $\epsilon_{\text{spot}} = 10^{-4}$, which is consistent with the value of 0.51 predicted by linear theory. Similar measurements at Mach 10 give $c_w^* = 0.4$ in the linear limit. As the amplitude is increased, the propagation speed of a disturbance along the shock decreases.

Conclusions

In this paper we provided a unified framework that has allowed us to deduce the scaling of shock characteristics (displacement and velocity) with respect to the amplitude of upstream disturbances and shock strength. These scalings were confirmed numerically for both the two-dimensional transverse vortex and the two-dimensional temperature spot for upstream Mach numbers up to 10. The velocity of the observed waves propagating along the shock correlates with that of a circular acoustic pulse originating from a source convecting at the mean downstream velocity. The triple points manifest themselves as singularities in the shock profiles. Their formation characteristics are different for the two types of upstream structures. When a high-intensity vortex interacts with a low-Mach-number shock, both singularities originate from a single point and result from excess shock curvature, which is inconsistent with flow states on either side of the shock. They form in pairs, propagating in opposite directions toward the freestream. A temperature spot of high intensity generates two triple points, symmetrically placed about $y = 0$. They also propagate in opposite directions toward the freestream. The separate effects of the pressure in the vortex core and the azimuthal velocity on the structure of the shock was investigated. At low Mach numbers nonlinear effects are dominated by convective effects, whereas at higher Mach numbers the effect of upstream density perturbation, also a nonlinear effect, on the downstream flow dominates.

References

[1]Erlebacher, G., Hussaini, M. Y., and Jackson, T. L., "Nonlinear Strong Shock-Vortex Interactions: A Shock-Fitted Approach," *Theoretical and Computational Fluid Dynamics*, Vol. 11, Nov. 1997, pp. 1–29.

[2]Hussaini, M. Y., and Erlebacher, G., "Numerical Simulations of Shock-Entropy Spot Interactions," *Proceedings of the Fifteenth International Conference on Numerical Methods in Fluid Dynamics*, edited by P. Kutler, J. Flores, and J.-J. Chattot, Lecture Notes in Physics, Springer–Verlag, New York, 1997, pp. 572–577.

[3]Hussaini, M. Y., and Erlebacher, G., "Interaction of an Entropy Spot with a Shock," *AIAA Journal*, Vol. 37, No. 3, 1998, pp. 346–356.

[4]Erlebacher, G., Hussaini, M. Y., and Shu, C.-W., "Interaction of a Shock with a Longitudinal Vortex," *Journal of Fluid Mechanics*, Vol. 337, April 1997, pp. 129–153.

[5]Zang, T. A., Hussaini, M. Y., and Bushnell, D. M., "Numerical Computations of Turbulence Amplification in Shock-Wave Interactions," *AIAA Journal*, Vol. 22, No. 1, 1984, pp. 13–21.

[6]Ribner, H. S., "Convection of a Pattern of Vorticity Through a Shock Wave," NASA TR-1164, Jan. 1954.

[7]Lasseigne, D. G., Jackson, T. L., and Hussaini, M. Y., "Nonlinear Interaction of a Detonation/Vorticity Wave," *Physics of Fluids*, Vol. 3, No. 8, 1991, pp. 1972–1979.

[8]Naumann, A., and Hermanns, E., "On the Interaction Between a Shock Wave and a Vortex Field," CP-131, AGARD, 1973.

[9]Dosanjh, D. S., and Weeks, T. M., "Interaction of a Starting Vortex as Well as a Vortex Street with a Traveling Shock Wave," *AIAA Journal*, Vol. 3, No. 2, 1965, pp. 216–223.

[10]Ellzey, J. L., Henneke, M. R., Picone, J. M., and Oran, E. S., "The Interaction of a Shock with a Vortex: Shock Distortion and the Production of Acoustic Waves," *Physics of Fluids*, Vol. 7, No. 1, 1995, pp. 172–184.

[11]Guichard, L., Vervisch, L., and Domingo, P., "Two-Dimensional Weak Shock-Vortex Interaction in a Mixing Zone," *AIAA Journal*, Vol. 33, No. 10, 1995, pp. 1797–1802.

[12]Courant, R., and Friedrichs, K. O., *Supersonic Flow and Shock Waves*, Vol. 21, Applied Mathematical Sciences, Springer–Verlag, New York, 1976.

[13]Ta'asan, S., and Nark, D., "An Absorbing Buffer Zone Technique for Acoustic Wave Propagation," AIAA Paper 95-0164, Jan. 1995.

[14]Carpenter, M. H., Gottlieb, D., and Abarbanel, S., "The Stability of Numerical Boundary Treatments for Compact High-Order Finite-Difference Schemes," *Journal of Computational Physics*, Vol. 180, No. 2, 1991, pp. 272–295.

[15]Carpenter, M. H., and Kennedy, C. A., "Fourth-Order 2N-Storage Runge-Kutta Schemes," NASA TM-109112, June 1994.

[16]Whitham, G. B., *Linear and Nonlinear Waves*, Wiley-Interscience, New York, 1974.

[17]Ribner, H. S., "Cylindrical Sound Wave Generated by Shock-Vortex Interaction," *AIAA Journal*, Vol. 23, No. 11, 1984, pp. 1708–1714.

P. Givi
Associate Editor